Role of Jahn-Teller distortion in the relative stability between the black and yellow phases of transition metal doped CsSnI₃ perovskites

Lucas G. Chagas [1], Juarez L. F. Da Silva,[2] and Matheus P. Lima [1,*]

[1]*Department of Physics, Federal University of São Carlos, 13565-905, São Carlos, São Paulo, Brazil*
[2]*São Carlos Institute of Chemistry, University of São Paulo, P.O. Box 780, 13560-970, São Carlos, São Paulo, Brazil*

Perovskite-based materials (ABX_3) show promise for photovoltaic applications; however, commercial use still encounters challenges, specifically Pb toxicity and structural instabilities of the active phases. A potential lead-free compound is $CsSnI_3$; nonetheless, the photoinactive yellow phase is energetically more favorable than the photoactive black phase. An undesired black→yellow phase transition implies structural instabilities, possibly explained by the Goldschmidt tolerance factor of 0.84. In this study, we employ theoretical calculations to investigate the impact of substitutional bivalent doping in the B sites of $CsSnI_3$ with $3d$ transition metals (TM) on tuning the relative energetic stability between the black and yellow phases. Our calculations are based on density functional theory, incorporating on-site Hubbard corrections for the TM $3d$ states. We observe an inversion of the relative stability between the yellow and black phases for dopings with Co, Cu, and Zn. We attribute the interphase relative energy to Jahn-Teller distortions at the doped octahedra, as the black and yellow phases exhibit distinct octahedral interconnections. For instance, the black phase has corner-shared octahedra, resulting in lower elastic costs for accommodating geometric distortions compared to the edge-shared octahedra in the yellow phase. The presented results highlight the influence of symmetry breaks on the stability of perovskite materials and have implications for other perovskite compositions.

I. INTRODUCTION

Halide perovskites (ABX_3) have emerged as promising materials for light absorbers in solar cells, as evidenced by their significant increase in power conversion efficiency (PCE) over the past decade. For example, from 3.8 % in 2009 [1] up to 25.5 % in 2020 [2]. However, real-life applications face two limitations: (i) limited phase stability at room temperature [3], e.g., moisture degradation [4], oxidative degradation [5], undesirable structural transitions [6], etc. [7]; (ii) and the demand for sustainable lead-free (nontoxic) photovoltaic devices with high PCE [8,9]. These challenges boosted a search for new compositions for perovskites, where the design of alternative materials becomes an important tool [10,11].

Pb-free perovskite such as $CsSnI_3$ appears as a promising candidate for composing the next generations of perovskite solar cells [12] given its excellent photophysical properties and resistance to decomposition by heat and ultraviolet irradiation [13]. The electronic energy band gap of 1.3 eV [14] approaches the optimum value claimed by Shockley–Queisser [15] for $p-n$ junction solar cells, resulting in a theoretical PCE exceeding 30 %. However, the highest certified PCE up to the present days is 10.1 % [16]. Despite the black phase $\gamma-CsSnI_3$ [17] being appropriate for employment in photovoltaic applications due to its suitable energy band gap, the unwanted yellow phase (photoinactive; $\delta-CsSnI_3$) has the lowest total energy [18], promoting the transition from

the black to the yellow phase. Thus the designing of stable $CsSnI_3$ solar cells demands mechanisms for controlling the relative stability between the black and yellow phases.

The substitutional doping at the bivalent B sites can contribute to improving the properties of black phase. For example, the replacement of Sn^{2+} metals by Ge^{2+} enhances the stability and the optoelectronic properties due to the decreasing of Sn^{2+} vacancy density, reduction of trap states, reduction of the effective mass of charge carriers, and also an increase in the absorption coefficient [19,20]. Moreover, doping of $CsSnI_3$ perovskites with Sb and Bi dopants replacing Sn atoms lowers the formation energy of the black phase above the yellow phase value. This mechanism increases the lifetime of the black phase under exposure to air [13]. Furthermore, doping perovskites with small Shannon radii transition-metal (TM) dopants stabilize the cubic phase of $CsPbI_3$ [21] (the Pb-toxic perovskite analogous to $CsSnI_3$ investigated here). However, an extensive exploration of the impact of transition-metal doping in the tin-based $CsSnI_3$ perovskite still lacks.

In this work, we investigate the relative stability between the black and yellow phases of $CsSnI_3$ under the replacement of Sn by all $3d$ transition-metal (TM) species, namely, Sc, Ti, V, Cr, Mn, Fe, Co, Ni, Cu, and Zn, at doping concentrations of 12.5 %. Our results were based on density functional theory (DFT) [22,23] calculations, including on-site Hubbard corrections to improve the description of the $3d$-state localization.

We found that the black phase is more stable than the yellow one for dopings with Co, Cu, and Zn. The specific doping with Cu atoms not only alters the relative energy between the black and yellow phases but also doubles its absolute

value compared to the undoped CsSnI$_3$ compound. We ascribe the interphase relative energy to Jahn-Teller distortions at the MI$_6$ octahedra, as the black and yellow phases have distinct octahedral interconnections, resulting in a higher energetic cost for distorting the octahedra in the yellow phase.

II. THEORETICAL APPROACH AND COMPUTATIONAL DETAILS

A. Total energy calculations

Our theoretical calculations were based on the spin-polarized DFT [22,23] framework, as implemented in the Vienna *ab initio* simulation package (VASP) [24,25], version 5.4.4, which employs the projected-augmented wave (PAW) method [26,27] to solve the Kohn-Sham (KS) equations using plane-wave basis functions. For the exchange-correlation energy functional, we employed the semilocal Perdew, Burke, and Ernzerhof [28] formulation, which faces challenges in providing an accurate description of localized transition-metal states, particularly by transition-metal dopants [29].

Thus, to improve the description of the TM 3d states within the CsSnI$_3$ compounds given their localized character, we adopted the effective Hubbard approach proposed by Dudarev *et al.* [30], where only the difference between the U on-site and J intersites Coulomb repulsion parameters is taken into account, i.e., $U_{\text{eff}} = U - J$ [31]. The most appropriate value for U_{eff} depends on factors such as the composition, geometric phase, local magnetic moments, and magnitude of the localization of the electronic states [32]. Furthermore, U_{eff} has weak transferability between different systems and should be adjusted case by case. Here, we considered the U_{eff} parameters only for the TM 3d states and two different values, namely, $U_{\text{eff}} = 3$ and 6.0 eV. Furthermore, we performed also PBE calculations, which is equivalent to $U_{\text{eff}} = 0$ eV. Therefore, the present calculations will helps to identify the role of the localization in the electronic, energetic, and structural properties [33,34].

To obtain the equilibrium structures, we optimized the stress-tensor and atomic forces using a higher plane-wave cutoff energy (590 eV). This specific value is twice the highest value of ENMAX (i.e., a parameter provided in the PAW projector files POTCAR) among all elements (i.e., copper). This choice is recommended due to the slow convergence of the stress-tensor as a function of the number of plane-waves. The formation energy (E_F) calculations also adopted this higher plane-wave cutoff energy, while the band structure calculations adopted the lower cutoff energy of 332 eV as this property is less sensitive to the plane-wave basis size. The Brillouin zone integration employed the Monkhorst-Pack scheme using a **k** mesh equivalent to 5×5×5 for the 1×1×1 unit cell.

To obtain the self-consistency electron density, a convergence total energy criteria of 1×10^{-6} eV was employed, while the equilibrium structures are reached once the atomic forces in every atom are smaller than 10 meV/Å. All structures were systematically generated through the optimization of lattice vectors and atomic positions for each U_{eff} value, ensuring a comprehensive exploration of the geometrical features. Moreover, the formation energy calculations for
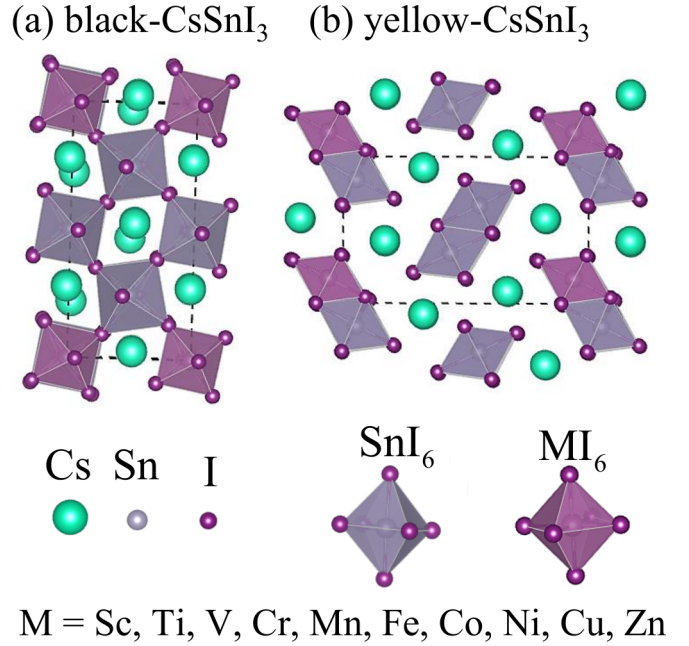
FIG. 1. Ball and octahedra representation of black and yellow CsSnI$_3$ supercells doped with 3d transition metals. The dashed lines indicate the unit cell, which is a 2×1×1 supercell doped with a single transition metal. Purple octahedral indicate the doping position.

charged systems ($q \neq 0$) include monopole and multipole corrections [35,36]. Our Ref. [37] (see also Refs. [38–46] therein) reports additional simulation details.

B. Modeling initial geometries

It has been reported that two competing phases exist at room temperature for the CsSnI$_3$ compound, as indicated by experimental studies [47,48] and theoretical calculations [6]. Both phases have orthorhombic structures, belong to the *Pnma* space group, and contain four formula units (f.u.) in the unit cell (4 Cs, 4 Sn, and 12 I atoms). These are (i) the $\gamma - $CsSnI$_3$ perovskite phase (black) with tilted, corner-shared octahedra forming an angle around 160° between the Sn $-$ I $-$ Sn bonds [49], which is a promising phase for photovoltaic applications [50]; and (ii) the $\delta - $CsSnI$_3$ nonperovskite phase (yellow) with edge-shared octahedra resulting in larger energy band gaps, making it unsuitable for photovoltaic applications [51]. It is crucial to emphasize that the distinct octahedral interconnections between the black and yellow phases are key to understanding the relative interphase stability discussed in this work. We extracted our initial lattice vectors and atomic positions for the black and yellow phases from the literature [43,52].

We employed the supercell approach to investigate transition-metal doping in CsSnI$_3$ compounds, using supercell sizes of 2×1×1 for both the black and yellow phases, as shown in Fig. 1. To construct these supercells, we replicated the unit cell in the direction of the shortest lattice vector and then replaced a single Sn atom with a 3d transition metal, resulting in simulation cells comprising 8 Cs, 7 Sn, 24 I, and one 3d TM atom. This structural model indicates a doping limit of 12.5% concentration, consistent with theoretical studies

TABLE I. Equilibrium lattice parameters (a_0, b_0, c_0, in angstroms) and fundamental electronic band gap (E_g, in eV) for two CsSnI3 phases along with literature results.

Phase	a_0	b_0	c_0	E_g	Ref.
black	8.703	8.948	12.590	0.95	this work
	8.643	8.688	12.378	-	[48][a]
	8.638	8.688	12.377	1.30	[49][a]
	8.625	8.918	12.469	0.83	[56][b]
yellow	4.823	10.813	18.084	2.23	this work
	4.763	10.350	17.684	2.55	[49][a]
	4.798	10.731	17.949	2.06	[56][b]

[a]Experimental data.
[b]Theoretical data.

that have been previously reported [53] and compatible with experimental explorations [54,55]. Importantly, the supercells for both the black and yellow phases have equal stoichiometry, enabling a direct comparison of their respective DFT total energies to assess relative stability.

III. RESULTS AND DISCUSSION

To better organize the data presentation, the results and discussions are divided into subsections. The first section, Sec. III A, compares our simulated results for lattice parameter and band gaps of undoped CsSnI$_3$ materials with data presented in the literature. The subsequent sections present results for CsSnI$_3$ doped with TM, whereas Sec. III B discusses the interphase relativity energy between the black and yellow phases with $U_{\text{eff}} = 0$, 3, and 6 eV, showing the trends with U_{eff} and which dopants promote the inversion of the most stable phase. Section III C shows the formation energy for different values of U_{eff} and different charge states (q). The subsection III D discusses the geometrical distortions resulting from the doping with TM, namely, the volume variations and the local octahedron distortions. Moreover, a characterization of the electronic structure is presented in Sec. III E, where we carried out band calculations to understand the oxidation state of each dopant and defect states eventually added inside the band gap. Finally, Sec. III F discusses the effects of impurity-impurity interaction, including magnetic interaction and effects of changing the distance between the TM dopants, considering only Ni, Co, and Fe.

A. Black and yellow bulk structures

Table I shows our optimized lattice parameters for the unit cell of the pristine black phase, a_0, b_0, and c_0, which are longer by 0.7 %, 3.0 %, and 1.7 %, respectively, if compared to the experimental values found for Yamada *et al.* [48]. Our calculations yield a fundamental energy band gap (fourth column in Table I) 26 % narrower than the experimentally measured value of 1.3 eV reported by [49] and 12 % wider than the theoretical value reported [56].

On the other hand, our simulations yielded lattice parameters (a_0, b_0, and c_0) for the unit cell of the pristine nonperovskite yellow phase that are 1.2 %, 4.5 %, and 2.3 % wider, respectively, than the reference experimental values reported by Chung *et al.* [49]. Our calculated band gap at the PBE level is only 12 % wider than the reported experimental value [48] and 8 % wider than the theoretical value [56].

Attempting to address the well-known issue of the underestimated band gaps with the plain PBE approach, we conducted additional test calculations using the hybrid HSE06 exchange-correlation functional, along with spin-orbit coupling (SOC) for the valence states. However, the resulting calculated band gaps at the PBE, HSE06, and PBE+SOC levels did not provide an effective correction to the experimental value (we report more details in Ref. [37]), resembling the results reported by Torres *et al.* [57] for CsPbI$_3$. Thus we decided to adopt uncorrected PBE simulations for CsSnI$_3$ materials due to their lowest cost in comparison with the other methodology we tested here.

We found a total energy of the pristine yellow phase lower by 13.5 meV/f.u. than the black one. This result corroborates experimental measures that indicate a spontaneous phase transition from the black (photoactive) to the yellow (photoinactive) phase. The competition between the black and the yellow phase was already explored for other perovskite materials such as CsPbI$_3$[58] and FAPbI$_3$ [59]. Our calculated band gaps at the PBE, HSE06, and PBE+SOC levels agree with the values reported by Su *et al.* [56].

B. Interphase relative energy

In this section, we investigate the impact of $3d$ transition-metal doping on the relative energetic stability between the black and yellow phases for CsSnI$_3$ through the relative energy ΔE_{tot}, i.e., the total energy difference between these two phases.

Figure 2 depicts the relative energy for $U_{\text{eff}} = 0$, 3, and 6 eV, representing the total energy of the doped black supercells relative to the doped yellow ones with the same dopant. Notably, a few particular transition metal dopings induce inversions of the relative energy, i.e., the black phase becomes energetically favored for dopings with Co, Cu, and Zn. Moreover, the incorporations of Fe and Ni with $U_{\text{eff}} = 0$ eV decrease the relative stability between the black and yellow phases without exchanging the interphase stability.

Focusing on changes due to the strength of the effective Hubbard correction, U_{eff}, it is worth noting variations in the absolute values of relative energies for all dopant species, without modifying the stablest phase. Specifically, the black phase becomes more stable only for dopings with Co, Cu, and Zn, regardless of the value for U_{eff}. Concerning their absolute values, we observed a general trend favoring the yellow phase; however, the variations in the relative energy values do not follow a consistent trend with the number of $3d$ electrons. This variation appears to be a unique feature of each dopant species. For example, the relative energy increases by almost $3\times$ for Sc doping with the increasing of U_{eff}, and remains almost constant for its neighbor in the periodic table, Ti. We attribute this behavior to the orbital occupations of $3d$ electrons that are specific to each transition metal species in the chemical environment of the host CsSnI$_3$ material.

From these relative energy results, we identified Cu doping as the most promising for stabilizing the black perovskite phase, as the relative energy between the black and yellow
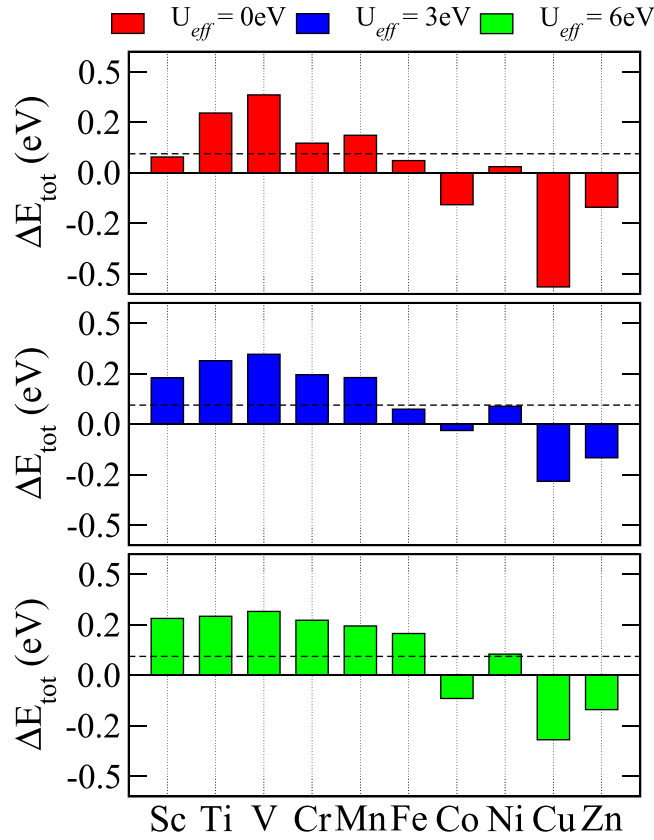
FIG. 2. Total energy of the black phase relative to the yellow phase for $Cs_8Sn_7(TM)_1I_{24}$ perovskites with $TM =$ Sc, Ti, V, Cr, Mn, Fe, Co, Ni, Cu, and Zn. These calculations adopts $2 \times 1 \times 1$ supercells. The dashed line indicates the undoped system.

phases decreases substantially. For example, it decreases from 94 meV (for the pristine system) to -566 meV (for Cu doping with $U_{eff} = 0$ eV), representing an exchange in stability with absolute values enhanced by a factor of $5\times$. These results demonstrate the effectiveness of small-radius transition-metal doping to handle the relative stability between the black and yellow phases.

C. Formation energies

Formation energies (E_F) provide insights into the feasibility and energetics of incorporating transition metal dopants into the crystal lattice. Additionally, the introduction of transition metal dopants can create localized levels within the energy band gap of perovskites. These levels can trap electrons or holes, allowing the existence of defects in varied charge states. Consequently, we evaluate the formation energy by

$$E_F(TM, q) = E_{\text{tot}}(TM, q) - E_p - \mu_{TM}$$
$$+ \mu_{\text{Sn}} + q(\mu_E + E_{\text{VBM}}), \qquad (1)$$

where $E_{\text{tot}}(TM, q)$ is the total energy for the perovskite doped with the transition-metal TM at the charge state $q = -1, 0,$ or $+1$. E_p is the total energy of the pristine system, μ_{TM} is the elemental chemical potential of the transition metal TM, calculated as the total energy per atom for the monoelemental
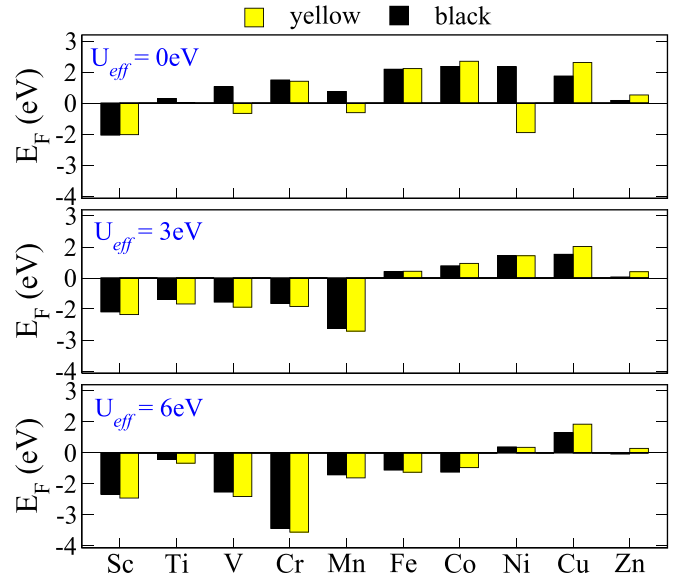
FIG. 3. Comparison of the formation energy of the black and yellow phase at different U_{eff}. $q = 0$ was used in both systems.

bulks (additional details are reported in Ref. [37]); μ_{Sn} is the elemental chemical potential for Sn, calculated as the total energy per atom of an Sn bulk in the diamond-like lattice; μ_E is the electronic chemical potential, which ranges from 0 up to the band gap value; and E_{VBM} is the eigenvalue energy of the top of the valence band taken from the pristine system. We apply this equation in good success in other semiconductor materials [60,61].

Figure 3 depicts E_F for all transition metals in the black and yellow phases for $U_{\text{eff}} = 0, 3,$ and 6 eV, focusing solely on neutral ($q = 0$) defects for clarity. There is substantial dependence of E_F on the value of U_{eff}, and we highlight three relevant features noted in this figure. (i) Firstly, it is worth noting that V, Mn, and Ni with $U_{\text{eff}} = 0$ exhibit a phase-dependent endothermic/exothermic behavior, as E_F is positive (endothermic) for the black phase and negative (exothermic) for the yellow one. However, the inclusion of the Hubbard correction ($U_{\text{eff}} > 0$) removes this feature, and only Zn remains with a phase-dependent endothermic/exothermic behavior, but with small values of E_F in comparison with room temperature. (ii) Fe and Co dopings clearly decrease E_F with the increasing of U_{eff}, up to reaching negative values for E_F (exothermic) with $U_{\text{eff}} = 6$ eV. We ascribe such behavior to localized states around the Fermi energy added by these dopants which was stronger affected by the Hubbard correction than the other states. (iii) The general trends of E_F for $U_{\text{eff}} = 3$ and 6 eV, such as the lowest E_F phase and its endothermic/exothermic character, resemble and are discrepant to the uncorrected ($U_{\text{eff}} = 0$) calculations, except for the aforementioned sign of E_F for Fe and Co. These results suggest that some degree of self-interaction correction results in more consistent outcomes.

Assuming that simulations for $U_{\text{eff}} = 3$ and 6 eV are more realistic, we can highlight some physical features from those as follows. (i) Low-filled $3d$ dopants (Sc, Ti, V, Cr, and Mn) result in exothermic (spontaneous) doping, whereas high-filled dopants (Ni, Cu, and Zn) result in endothermic ones.
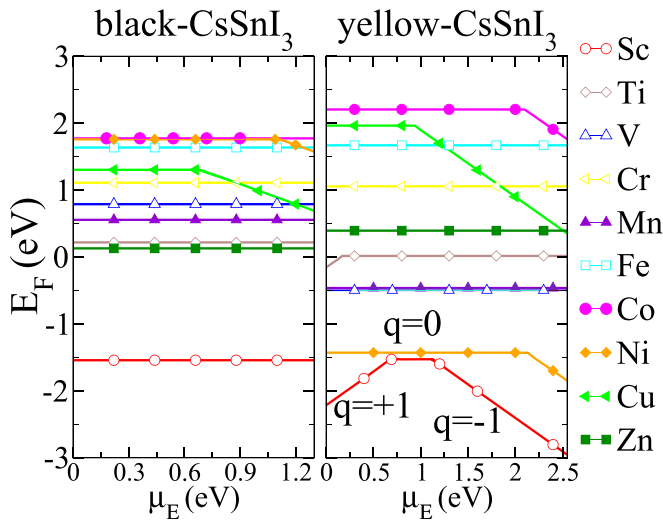
FIG. 4. Formation energies as a function of the electronic chemical potential (μ_E) for black and yellow doped CsSnI$_3$ materials using $U_{\text{eff}} = 0$ eV. Plots show only the lowest energy charge states.

FIG. 5. Geometrical parameters for the black phase of CsSnI$_3$ doped with $3d$ transition metals using $U_{\text{eff}} = 3$ eV. Volume per unit formula; effective coordination number (ECN) in units of the number of nearest neighbor (NNN); and average M–I bond lengths, where TM is the doping $3d$ transition metal. Dashed lines indicate the data for undoped systems.

Particularly, Fe and Co doping present exothermic (endothermic) E_F with $U_{\text{eff}} = 3$ eV (6 eV). The sign of the formation energy (negative or positive) provides information about the ease of the doping process, and negative values indicate an exothermic spontaneous doping process. (ii) All these low-filled dopants easily dope the yellow phase, as demonstrated by their lowest E_F than the black phase. The converse is also true, i.e., the high-filled dopants Co, Ni, Cu, and Zn have the lowest E_F for the black than the yellow phase. Particularly, the Fe doping changes the lowest E_F phase with the U_{eff} increase. Such an energetically favored doping of the black phase for high-filled dopants is key to handling the relative phase stability between the black and yellow phases.

We also conduct a screening of energetically favorable charge states by evaluating Eq. (1) for all dopants with $q = -1$, 0, and $+1$ for $U_{\text{eff}} = 0$ eV, as shown in Fig. 4. Regarding the charge states, most dopants remain neutral in a wide range of electronic chemical potential. For the black phase, only Ni and Cu can access the charge state $q = -1$ (with one trapped electron) for chemical potentials close to the bottom of the conduction band. Moreover, all dopants can access the neutral charge state for the yellow phase. However, only Sc and Ti can access the charge state $q = +1$ for an electronic chemical potential close to the top of the valence band, while only Sc, Co, Ni, and Cu can access the charge state $q = -1$ if the electronic chemical potential is close to the bottom of the conduction band.

Henceforth, the presented results focus only on simulations with $U_{\text{eff}} = 3$ eV, as the formation energy calculations demonstrate uniformity of results when including effective Hubbard repulsion terms.

D. Local structural distortions

A motivation for stabilizing the black phase of ABX_3 perovskites upon transition-metal substitutional doping at the B site resides in the Goldschmidt tolerance factor, i.e., $t = \frac{r_{AX}}{\sqrt{2}\,r_{BX}}$, where r_{AX} (r_{BX}) is the A–X (B–X) bond length.

An ideal cubic perovskite has $t = 1$, and symmetric cubic phases occurs for t in the range $0.9 - 1$. Stable prerovskites, however, with some octahedral distortions occur for $0.81 < t < 0.9$, and strong lattice distortions are expected if the Goldschmidt tolerance factor fall out of the range 0.81–1.11, resulting in phase transitions and other structural instabilities [62–64].

Figure 5 presents geometrical parameters calculated from the optimized geometries of CsSnI$_3$ doped with $3d$ transition metals at the B site for both black and yellow phases. Here, we exclusively investigate neutral ($q = 0$) defects with $U_{\text{eff}} = 3$ eV. The yellow phase exhibits the expected volume decrease for all dopants. However, in the doped structures of the black phase, the volume decreases (as expected) for all dopants, except Fe, Co, and Zn. This unexpected volume increase draws attention to potential internal octahedral distortions. That is, the replacement of B atoms with smaller radius dopants resulting in volume increases due to symmetry breaks in the six $B - $ I bonds of the BI$_6$ octahedra, thereby breaking the ideal bond length relationships assumed by Goldschmidt in its tolerance factor. Thus the Goldschmidt tolerance factor becomes less effective in predicting perovskite phases [65,66] for structures with internal distortions, such as Jahn-Teller symmetry breaks [67], as local octahedral distortions modify the ideal interatomic bond length relations adopted by Goldschmidt.

In this context, the effective coordination number (ECN) at the B site measures the internal octahedral distortions, accounting for fluctuations in the B–X bond lengths. The effectiveness of ECN lies in its ability to consider deviations from perfect octahedral coordination (ECN = 6 NNN), offering a more nuanced understanding of the structural characteristics in perovskite materials. The middle panel of Fig. 5 illustrates the effective coordination number (ECN) for the transition metal in all investigated systems. For reference, the pristine black CsSnI$_3$ structure has an ECN of 5.67 NNN, with this subtle reduction in the ideal value of 6 NNN originating from small octahedral deformations due to the particular tilting of the octahedra in the yellow phase [49]. The black phase doped with Sc, Ti, V, and Cr has ECN values close to 6 NNN, indicating MI$_6$ octahedra approaching to the ideal cubic symmetry. However, the ECN decreases to values as low as three (3) as the number of $3d$ electrons increases, demonstrating strong internal octahedral distortions for dopants with more than five electrons in the $3d$ shell.

We also assessed the local geometrical distortions by examining the average distance between the doping transition metal and its six surrounding iodine atoms, denoted as d_{av} and shown in the bottom panel of Fig. 5. In both the black and yellow phases, there is a reduction in d_{av} for dopants with five or fewer electrons in the $3d$ shell, as expected due to the smaller atomic radii of these transition metals compared to the replaced Sn. However, differences between the phases appear for the remaining atoms. In the black phase, Fe, Co, and Ni have d_{av} values close to that of the pristine system, while Cu and Zn exceed it. In contrast, the yellow phase maintains the short d_{av} in comparison with the pristine system for Fe, Co, Ni, and Zn, but increases it for Cu. Here, we highlight the higher increase of d_{av} associated with the most prominent changes in the relative energy for Cu doping. The aforementioned analysis of volume, ECN, and d_{av}, correlated with the energetic analysis presented in Secs. III B and III C, highlights the significance of geometrical distortions in determining the relative stability between the black and yellow phases.

Jahn-Teller distortions in perovskites are ascribed to lone pairs at the atoms occupying the B site [65]. The lone pairs present in transition-metals with more than five electrons in the $3d$ shell favor internal distortions at MI$_6$ octahedronsm. These Jahn-Teller distortions also occur in other perovskite systems, as germanium-based perovskites, i.e., previous reports demonstrated that the GeX_6 octahedrons (X = Cl, Br, and I) spontaneously distort in such a way that three GeX bonds elongate and the remaining three GeX bonds shorten, from a theoretical [66] and experimental [68] approaches.

In general, the ECN values are quite similar for both black and yellow phases doped with transition metals with five or fewer electrons in the $3d$ shell. However, structural distortions promote differences for other dopants with more electrons. Correlating the structural and the energetic data, it is possible to note that ideal octahedra favor the yellow phase, whereas distorted octahedrons favor the black perovskite phase. Moreover, distortions occurs in transition metals with more than five electrons in the $3d$ shell due to Jahn-Teller distortions. We ascribe this result to different octahedra-interconnection between the black and yellow phases, i.e., the black perovskite has corner-shared octahedrons. Thus local distortions generate
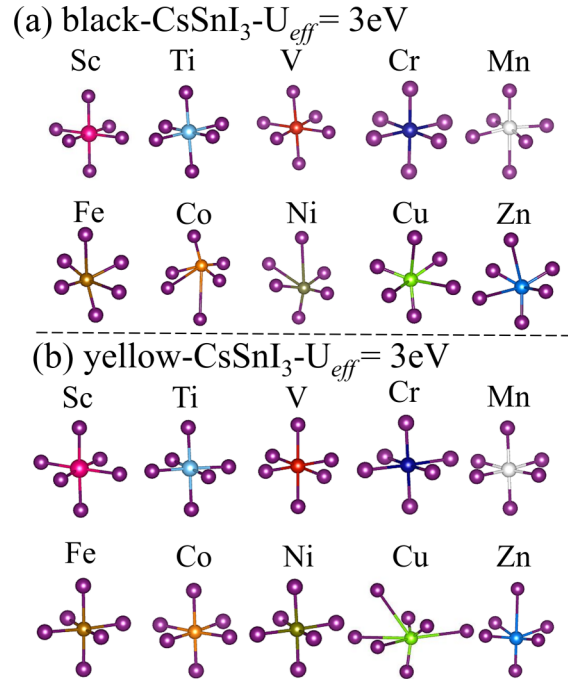
FIG. 6. Ball and stick representation of the $3d$ TM and their surrounding I atoms for doped CsSnI$_3$ black perovskites. The bond lengths adopt a cutoff distance of 5.0 Å.

bending in the octahedra surrounding it. However, the yellow phase has edge-shared octahedra, and local distortions mostly modify bond lengths in the surrounding region, leading to a higher elastic cost in comparison with the black phase.

The Jahn-Teller distortions cause local deformations around the transition metal dopant that manifest in the atomic positions of the MI$_6$ octahedra. Figure 6 presents a ball-and-stick model for all dopants (TM) and the six iodine atoms surrounding them. Specifically, these geometries consider fully optimized structures with $U_{eff} = 3$ eV; nevertheless, a comprehensive table detailing the N-I bond lengths for various simulated U_{eff} values is available in our supplementary material [37]. These distorted MI$_6$ octahedra can be correlated with the geometrical descriptors presented in Fig. 5. For instance, dopants with five or fewer electrons in the $3d$ shell exhibit regular MI$_6$ octahedra in both black and yellow phases. The remaining dopants induce more pronounced geometrical distortions in the black phase compared to the yellow one, except for Cu, where the MI$_6$ octahedra are significantly more distorted in the yellow phase. Moreover, the distorted octahedra for dopants with more than five electrons in the $3d$ shell not only alter the bond lengths but also modify the internal angles, contributing to a volume increase, despite the dopants having shorter atomic radii.

E. Electronic properties

Transition metal dopants influence the electronic structure around the Fermi level, impacting key properties in the context of photovoltaics, such as optical [57,69] and transport [70] properties, and an analysis of the electronic band structure provides insights into numerous relevant features. Figure 7 depicts the spin-resolved band structures generated with
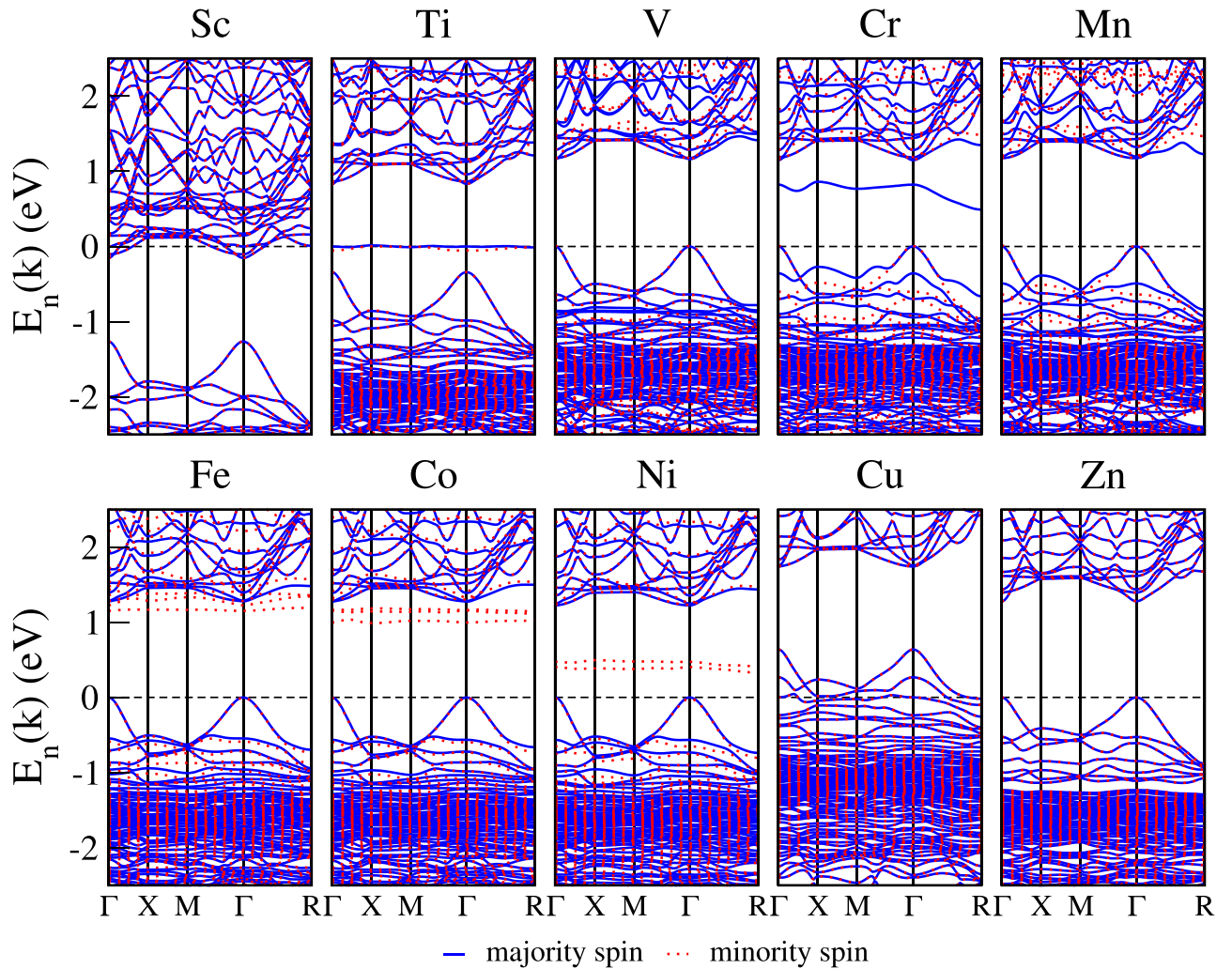
FIG. 7. Electronic band structures for black CsSnI$_3$ perovskite doped with $3d$ transition-metals with $U_{\text{eff}} = 3$ eV. Blue (red) circles are fatbands of transition metal states for the majority (minority) spin. The labels above each panel indicate the dopant and the charge state. The black dashed line indicates states below which are occupied, and those above are unoccupied.

effective Hubbard correction at $U_{\text{eff}} = 3$ eV, expected to correct the results of plain-PBE simulations. In this section, we focus solely on the doped black phase due to its greater importance for photovoltaic applications. However, supplementary data for the yellow phase and other values of U_{eff} can be found in in Ref. [37].

From these band structures, we can deduce the number of oxidation states (NOX) for each dopant. Sc doping positions the Fermi energy inside the conduction band, indicating that this dopant contributes more electrons than the Sn it replaces. This positioning of the Fermi energy, associated with the hybridization of $4s^2 3d^1$ valence electrons with the conduction band, is consistent with NOX = 3. For Ti doping, two localized bands with opposite spins appear above the valence band maximum (VBM), along with other filled transition metal states hybridizing with the valence band, indicating NOX = 2. However, the Fermi energy is pinned at the flat localized defect bands, as these bands are half-filled. Dopings with V, Mn, and Zn result in band structures without the addition of localized states inside the band gap, which is located at the Γ point. Conversely, Cr, Fe, Co, and Ni dopings introduce

unfilled localized states within the band gap, potentially creating charge traps that affect (decrease) the charge flow. For all these dopants (Ti, V, Cr, Mn, Fe, Co, Ni, and Zn), despite the addition of states inside the band gap in some cases, the Fermi level lies between the VBM and the conduction band minimum (CBM), consistently indicating NOX = 2. The Cu doping state results in the Fermi energy located inside the valence band, agreeing with previour reports [71]. In this case, the effective electronic configuration ($3d^{10} 4s^1$) and the Fermi energy positioning is consistent with NOX = 1.

The effective Hubbard correction (PBE+U) significantly influences the position of localized states within the band gap. A comparison between corrected and noncorrected electronic band structures reveals that the Hubbard correction shifts the flat defect states for V doping from the bottom of the conduction band to the middle region of the band gap. Furthermore, PBE + U correction eliminates the band gap's localized states for Cr doping, effectively cleaning the band gap.

We also calculated the band gap by the energy difference between VBM nd CBM without consider the localized defect states as 1.11 eV (Sc), 1.17 eV (Ti), 1.15 eV (V), 1.14 eV

(Cr), 1.16 eV (Mn), 1.28 eV (Fe), 1.28 eV (Co), 1.22 eV (Ni), 1.10 eV (Cu), and 1.28 eV (Zn). We ascribe the band gap increase with respect to the pristine perovskite ($E_g = 0.95$ eV, which is on the same level as for PBE + U with $U_{\text{eff}} = 3$ eV) to two reasons: (i) variations in the volume, and (ii) coupling between the electronic states of the valence and conduction bands due to Jahn-Teller effects. Similar effects were reported for the Dias *et al.* for the CsGeX_3 (X = Cl, Br, I) [66].

Considering only the dopants promoting the inversion of the energetic stability between the black and yellow phases, only Zn has a clean band gap without localized defect levels. As these localized levels can result in charge recombinations reducing the PCE, we motivate the experimentalists to realize the doping with Zn ions to avoid undesirable transition from the black to the yellow phase, maintaining the electronic structure without localized levels inside the band gap region.

F. Role of impurity-impurity interactions

Local magnetic moments often arise from transition-metal-doped semiconductor materials, such as perovskites, forming arrays of magnetically coupled paramagnetic centers [72]. In this context, factors such as the magnetic alignment [73] (ferromagnetic, FM, or antiferromagnetic, AFM) and the geometric arrangement between the local magnetic moments [74,75] influence their energetic and electronic properties. This section explores these features through simulations of geometries with distinct dopant arrangements and magnetic orderings. The investigations focus specifically on the dopants Fe, Co, and Ni due to their high potential for generating local magnetic moments in other systems [76,77]. The results presented in this section also test the robustness of the findings from the previous sections, which employ geometries consisting of a supercell with a single dopant at concentrations of 12.5 %.

We constructed three distinct geometric arrangements for each dopant. (i) We duplicated the optimized geometries of the doped supercells with 40 atoms (containing one dopant among them) in the direction of the shortest lattice vector. This resulted in a supercell with 80 atoms containing two dopants around 8.5 Å one each other. And, the remaining two geometries were constructed from an undoped (pristine) supercell with 80 atoms which is equivalent to the first structure and we subsequently replaced two Sn by transition metals in (ii) neighboring (closest) octahedra. The shortest distance between these dopants are around 6 Å; and (iii) octahedra with the farthest possible positions one each other (around 13 Å, taking into consideration the lattice periodicity). Each one of these three structures where fully relaxed by optimized both the lattice parameters and atomic positions up to reach a tolerance criterion. For those calculations, we also employ initial magnetic ordears FM and AFM, resulting in six calculations for each dopant.

Table II summarizes the results of these simulations. Finite local magnetic moments m_l emerge in all dopants and are consistent with the electron fillings of $3d^6$, $3d^7$, and $3d^8$ for Fe, Co, and Ni, respectively. Moreover, the highest total energy difference ΔE_{tot} between structures with equivalent values of $d_{TM\text{-}TM}$ is 45 meV for Fe at intermediate distances ($\sim$8.5 Å), with FM being the lowest energy configuration. For other

TABLE II. Magnetic interactions between Fe, Co, Ni extracted from simulations of supercells containing 80 atoms with two dopants with $U_{\text{eff}} = 3$ eV. The table presents the shortest distance between the dopants ($d_{M\text{-}M}$), the magnetic configuration (FM or AFM), the average local magnetic moment for each dopant (m_l), the total energy per dopant relative to the lowest energy configuration (ΔE_{tot}), and the average effective coordination number for the transition metal site (ECN_{av}^B). Bolded data indicate the lowest energy simulation for each dopant.

M	$d_{TM\text{-}TM}$ (Å)	configuration	m_l (μ_B)	ΔE_{tot} (eV)	ECN_{av}^B (NNN)
Fe	6.128	FM	3.58	0.041	3.95
Fe	5.905	AFM	3.58	0.036	4.13
Fe	8.644	**FM**	3.57	0.000	3.98
Fe	8.588	AFM	3.58	0.045	3.98
Fe	13.348	FM	3.58	0.040	4.06
Fe	13.712	AFM	3.59	0.052	4.54
Co	6.332	FM	2.54	0.064	3.91
Co	6.282	AFM	2.54	0.056	3.91
Co	8.673	FM	2.54	0.000	3.98
Co	8.673	**AFM**	2.54	0.000	3.98
Co	13.135	FM	2.54	0.098	3.98
Co	13.109	AFM	2.54	0.092	3.98
Ni	6.203	FM	1.43	0.025	3.93
Ni	6.052	AFM	1.43	0.012	3.97
Ni	8.617	FM	1.44	0.001	3.98
Ni	8.614	**AFM**	1.44	0.000	3.98
Ni	13.397	FM	1.43	0.023	4.08
Ni	13.395	AFM	1.43	0.022	4.08

dopants and $d_{TM\text{-}TM}$, this energy does not exceed 13 meV for Ni doping in neighboring octahedra ($d \sim 6$ Å), where the AFM configuration has the lowest energy. This analysis shows that the total energy difference between FM and AFM configurations does not correlate with d_{TM-TM} and is low in comparison with room temperature ($k_B T \approx 25$ meV), indicating that magnetic order does not dominate the interactions between the dopants.

As the geometries of the systems with 80 atoms in the unit cell, doped with two transition metals at intermediate distances ($\sim$8.5 Å), were constructed from the fully optimized geometries of systems with 40 atoms and only one transition metal, a comparison between the properties of these systems and the remaining ones provides insights into the robustness of the results presented in the previous sections. In this context, the lowest energy configuration for all systems with dopants at intermediate distances demonstrates the energetic likelihood and, consequently, the suitability of these geometries (with 40 atoms containing one dopant) for theoretical explorations. Moreover, Fe doping results in an energetic preference for the FM phase, whereas Co and Ni have FM and AFM magnetic phases degenerate in energy for this intermediate distance. Thus these tests with larger unit cells allowing varied magnetic interactions support the validity of the results presented in the previous sections of this manuscript.

Intriguingly, an apparent lack of correlation between ΔE_{tot} and the remaining properties is observed in the data presented in Table II. The weak magnetic coupling between impurities

is not surprising, given that the minimum $TM - TM$ distance is as long as 5.9 Å. This long distance, coupled with dielectric screening and the presence of at least one iodine atom between the dopants, results in a short-range magnetic interaction. However, differences in values for different configurations suggest a hidden key factor. We attribute this peculiar behavior to Jahn-Teller distortions, where symmetry breaks in the doped MI_6 octahedra extend to neighboring SnI_6 ones. The overall lattice distortion appears to play a more significant role in governing ΔE_{tot} than the magnetic ordering.

IV. CONCLUSIONS

Herein, we explore the relative stability between the black and yellow phases and their electronic properties under substitutional doping with $3d$ transition metals (TM = Sc, Ti, V, Cr, Mn, Fe, Co, Ni, Cu, and Zn) at Sn sites. Our exploration uses *ab initio* calculations based on density functional theory with the PBE parametrization for the exchange-correlation energy functional and includes the effective Hubbard correction to $3d$ transition metal states. Our analysis combines (i) total energy calculations; (ii) an analysis of the local distortions through bond lengths, volumes, and effective-coordination-number evaluation; (iii) a geometrical analysis; and (iv) investigation of $TM - TM$ interactions, concluding that the Jahn-Teller distortion induced by transition metal doping rules the relative stability between the black and yellow phases.

Dopants with more than five electrons in the $3d$ shell tend to favor the black phase, except for Fe doping with $U_{\text{eff}} = 6$ eV. In particular, the incorporation of Co, Cu, and Zn results in a photoactive black phase with lower energy than the photoinactive yellow phase. The Cu doping highlights as it not only exchanges the most active phase but also increases their total energy difference by a few times in comparison with the undoped system. However, this dopant introduces states inside the band gap region that could result in charge recombination, reducing the PCE. However, the doping with Zn ions also exchanges the relative stability maintaining a clean band gap region without defect states. Our investigation on the $TM - TM$ interactions demonstrates that the local distortion effects overcome the magnetic interaction between the dopants as well as the effects of changing the periodicity pattern. Thus Jahn-Teller distortions are a dominating stability factor for perovskite materials doped with transition metals.

The presented results provide a foundation for future photovoltaic applications with transition metal doping, demonstrating the relevance of local geometrical distortions for phase transitions in perovskites, guiding future investigations.

[1] A. Kojima, K. Teshima, Y. Shirai, and T. Miyasaka, Organometal halide perovskites as visible-light sensitizers for photovoltaic cells, J. Am. Chem. Soc. **131**, 6050 (2009).

[2] T. N. R. E. L. (NREL), The best cell-efficiency chart, https://www.nrel.gov/pv/assets/pdfs/cell-pv-eff-emergingpv-rev210726.pdf (2020).

[3] Y. An, J. Hidalgo, C. A. R. Perini, A.-F. Castro-Méndez, J. N. Vagott, K. Bairley, S. Wang, X. Li, and J.-P. Correa-Baena, Structural stability of formamidinium- and cesium-based halide perovskites, ACS Energy Lett. **6**, 1942 (2021).

[4] K. J. Xu, R. T. Wang, A. F. Xu, J. Y. Chen, and G. Xu, Hysteresis and instability predicted in moisture degradation of perovskite solar cells, ACS Appl. Mater. Interfaces **12**, 48882 (2020).

[5] L. Wang, Z. Wang, H. Li, B. Chang, L. Pan, Z. Xie, and L. Yin, Pseudohalide anions to suppress oxidative degradation for efficient formamidinium-based Sn–Pb halide perovskite solar cells, ACS Appl. Mater. Interfaces **14**, 18302 (2022).

[6] E. L. da Silva, J. M. Skelton, S. C. Parker, and A. Walsh, Phase stability and transformations in the halide perovskite CsSnI₃, Phys. Rev. B **91**, 144107 (2015).

[7] A. Aftab and M. I. Ahmad, A review of stability and progress in tin halide perovskite solar cell, Solar Energy **216**, 26 (2021).

[8] J. Li, J. Duan, X. Yang, Y. Duan, P. Yang, and Q. Tang, Review on recent progress of lead-free halide perovskites in optoelectronic applications, Nano Energy **80**, 105526 (2021).

[9] A. Bibi, I. Lee, Y. Nah, O. Allam, H. Kim, L. N. Quan, J. Tang, A. Walsh, S. S. Jang, E. H. Sargent, and D. H. Kim, Lead-free halide double perovskites: Toward stable and sustainable optoelectronic devices, Mater. Today **49**, 123 (2021).

[10] X. Jiang and W.-J. Yin, High-throughput computational screening of oxide double perovskites for optoelectronic and photocatalysis applications, J. Energy Chem. **57**, 351 (2021).

[11] J. Kim, E. Kim, and K. Min, Synthesizable double perovskite oxide search via machine learning and high-throughput computational screening, Adv. Theory Simul. **4**, 2100263 (2021).

[12] G. Wang, J. Chang, J. Bi, M. Lei, C. Wang, and Q. Qiao, Inorganic CsSnI₃ perovskite solar cells: The progress and future prospects, Solar RRL **6**, 2100841 (2022).

[13] M. Lee, B. Yoo, J. Im, T. Hyeon, and I. Chung, Electronic band engineering via MI₃ (M = Sb, Bi) doping remarkably enhances the air stability of perovskite CsSnI₃, ACS Appl. Energy Mater. **3**, 10477 (2020).

[14] X. Qiu, B. Cao, S. Yuan, X. Chen, Z. Qiu, Y. Jiang, Q. Ye, H. Wang, H. Zeng, J. Liu, and M. G. Kanatzidis, From unstable CsSnI₃ to air-stable Cs₂SnI₆: A lead-free perovskite solar cell light absorber with band gap of 1.48eV and high absorption coefficient, Sol. Energy Mater. Sol. Cells **159**, 227 (2017).

[15] W. Shockley and H. J. Queisser, Detailed balance limit of efficiency of p-n junction solar cells, J. Appl. Phys. **32**, 510 (1961).

[16] T. Ye, X. Wang, K. Wang, S. Ma, D. Yang, Y. Hou, J. Yoon, K. Wang, and S. Priya, Localized electron density engineering

for stabilized B − γ CsSnI$_3$-based perovskite solar cells with efficiencies >10%, ACS Energy Lett. **6**, 1480 (2021).

[17] L. Dimesso, C. Das, M. Stöhr, T. Mayer, and W. Jaegermann, Properties of cesium tin iodide (Cs − Sn − I) systems after annealing under different atmospheres, Mater. Chem. Phys. **197**, 27 (2017).

[18] S. Zhou, S. Zhu, J. Guan, R. Wang, W. Zheng, P. Gao, and X. Lu, Confronting the air instability of cesium tin halide perovskites by metal ion incorporation, J. Phys. Chem. Lett. **12**, 10996 (2021).

[19] M. Liu, H. Pasanen, H. Ali-Löytty, A. Hiltunen, K. Lahtonen, S. Qudsia, J.-H. Smått, M. Valden, N. V. Tkachenko, and P. Vivo, B-site co-alloying with germanium improves the efficiency and stability of all-inorganic tin-based perovskite nanocrystal solar cells, Angew. Chem. Int. Ed. **59**, 22117 (2020).

[20] M.-G. Ju, J. Dai, L. Ma, and X. C. Zeng, Lead-free mixed tin and germanium perovskites for photovoltaic application, J. Am. Chem. Soc. **139**, 8038 (2017).

[21] A. Swarnkar, W. J. Mir, and A. Nag, Can B-site doping or alloying improve thermal- and phase-stability of all-inorganic CsPbX$_3$ (X = Cl, Br, I) perovskites?, ACS Energy Lett. **3**, 286 (2018).

[22] P. Hohenberg and W. Kohn, Inhomogeneous electron gas, Phys. Rev. **136**, B864 (1964).

[23] W. Kohn and L. J. Sham, Self-consistent equations including exchange and correlation effects, Phys. Rev. **140**, A1133 (1965).

[24] G. Kresse and J. Hafner, *Ab initio* molecular dynamics for open-shell transition metals, Phys. Rev. B **48**, 13115 (1993).

[25] G. Kresse and J. Furthmüller, Efficient iterative schemes for *ab initio* total-energy calculations using a plane-wave basis set, Phys. Rev. B **54**, 11169 (1996).

[26] P. E. Blöchl, Projector augmented-wave method, Phys. Rev. B **50**, 17953 (1994).

[27] G. Kresse and D. Joubert, From ultrasoft pseudopotentials to the projector augmented-wave method, Phys. Rev. B **59**, 1758 (1999).

[28] J. P. Perdew, K. Burke, and M. Ernzerhof, Generalized gradient approximation made simple, Phys. Rev. Lett. **77**, 3865 (1996).

[29] E. Ruiz, S. Alvarez, J. Cano, and V. Polo, About the calculation of exchange coupling constants using density-functional theory: The role of the self-interaction error, J. Chem. Phys. **123**, 164110 (2005).

[30] S. L. Dudarev, G. A. Botton, S. Y. Savrasov, C. J. Humphreys, and A. P. Sutton, Electron-energy-loss spectra and the structural stability of nickel oxide: An LSDA+U study, Phys. Rev. B **57**, 1505 (1998).

[31] R. Micnas, J. Ranninger, and S. Robaszkiewicz, An extended Hubbard model with inter-site attraction in two dimensions and high-T$_c$ superconductivity, J. Phys. C **21**, L145 (1988).

[32] R. Tesch and P. M. Kowalski, Hubbard U parameters for transition metals from first principles, Phys. Rev. B **105**, 195153 (2022).

[33] H. J. Kulik, M. Cococcioni, D. A. Scherlis, and N. Marzari, Density functional theory in transition-metal chemistry: A self-consistent Hubbard U approach, Phys. Rev. Lett. **97**, 103001 (2006).

[34] F. F. H. Aragón, L. Villegas-Lelovsky, L. Cabral, M. P. Lima, A. Mesquita, and J. A. H. Coaquira, Tuning the magnetic properties of Sn$_{1-x-y}$Ce$_{4+x}$Ce$_{3+y}$O$_2$ nanoparticles: An

experimental and theoretical approach, Nanoscale Adv. **3**, 1484 (2021).

[35] G. Makov and M. C. Payne, Periodic boundary conditions in *ab initio* calculations, Phys. Rev. B **51**, 4014 (1995).

[36] J. Neugebauer and M. Scheffler, Adsorbate-substrate and adsorbate-adsorbate interactions of Na and K adlayers on Al(111), Phys. Rev. B **46**, 16067 (1992).

[37] See Supplemental Material at http://link.aps.org/supplemental/10.1103/PhysRevB.109.014106 for further details about (i) investigated crystal phases, (ii) convergence tests, and (iii) simulation data details.

[38] C. Yu, Z. Chen, J. J. Wang, W. Pfenninger, N. Vockic, J. T. Kenney, and K. Shum, Temperature dependence of the band gap of perovskite semiconductor compound CsSnI$_3$, J. Appl. Phys. **110**, 063526 (2011).

[39] J. A. Steele, H. Jin, I. Dovgaliuk, R. F. Berger, T. Braeckevelt, H. Yuan, C. Martin, E. Solano, K. Lejaeghere, S. M. J. Rogge, C. Notebaert, W. Vandezande, K. P. F. Janssen, B. Goderis, E. Debroye, Y.-K. Wang, Y. Dong, D. Ma, M. Saidaminov, H. Tan *et al.*, Thermal unequilibrium of strained black CsPbI$_3$ thin films, Science **365**, 679 (2019).

[40] W. Ahmad, J. Khan, G. Niu, and J. Tang, Inorganic CsPbI$_3$ perovskite-based solar cells: A choice for a tandem device, Solar RRL **1**, 1700048 (2017).

[41] I. Chung, B. Lee, J. He, R. P. H. Chang, and M. G. Kanatzidis, All-solid-state dye-sensitized solar cells with high efficiency, Nature (London) **485**, 486 (2012).

[42] R. X. Yang and L. Z. Tan, Understanding size dependence of phase stability and band gap in CsPbI$_3$ perovskite nanocrystals, J. Chem. Phys. **152**, 034702 (2020).

[43] Z. Zhao, J. Wu, F. Fang, T. Li, Y. Zhou, and J. Wang, The mechanism of the stability improvement of the Bγ-CsSnI$_3$ perovskite doped with fluorine, Mater. Res. Express **6**, 125534 (2019).

[44] Z. Xiao, H. Lei, X. Zhang, Y. Zhou, H. Hosono, and T. Kamiya, Ligand-hole in [SnI$_6$] unit and origin of band gap in photovoltaic perovskite variant Cs$_2$SnI$_6$, Bull. Chem. Soc. Jpn. **88**, 1250 (2015).

[45] Z. Xiao, Y. Zhou, H. Hosono, and T. Kamiya, Intrinsic defects in a photovoltaic perovskite variant Cs$_2$SnI$_6$, Phys. Chem. Chem. Phys. **17**, 18900 (2015).

[46] J. Wu, Z. Zhao, and Y. Zhou, The optoelectronic properties improvement of double perovskites Cs$_2$SnI$_6$ by anionic doping (F$^-$), Sci. Rep. **12**, 935 (2022).

[47] P. Mauersberger and F. Huber, Structure of caesium triiodostannate(II), Acta Cryst. B **36**, 683 (1980).

[48] K. Yamada, S. Funabiki, H. Horimoto, T. Matsui, T. Okuda, and S. Ichiba, Structural phase transitions of the polymorphs of CsSnI$_3$ by means of rietveld analysis of the x-ray diffraction, Chem. Lett. **20**, 801 (1991).

[49] I. Chung, J.-H. Song, J. Im, J. Androulakis, C. D. Malliakas, H. Li, A. J. Freeman, J. T. Kenney, and M. G. Kanatzidis, CsSnI$_3$: Semiconductor or metal? High electrical conductivity and strong near-infrared photoluminescence from a single material. High hole mobility and phase-transitions, J. Am. Chem. Soc. **134**, 8579 (2012).

[50] K. P. Marshall, M. Walker, R. I. Walton, and R. A. Hatton, Enhanced stability and efficiency in hole-transport-layer-free CsSnI$_3$ perovskite photovoltaics, Nat. Energy **1**, 16178 (2016).

[51] L.-y. Huang and W. R. L. Lambrecht, Electronic band structure, phonons, and exciton binding energies of halide perovskites

CsSnCl$_3$, CsSnBr$_3$, and CsSnI$_3$, Phys. Rev. B **88**, 165203 (2013).

[52] D. B. Straus, S. Guo, and R. J. Cava, Kinetically stable single crystals of perovskite-phase CsPbI$_3$, J. Am. Chem. Soc. **141**, 11435 (2019).

[53] F. B. Selim, A. Kabir, and S. S. Nishat, Effects of transition metal doping on CsGeBr$_3$ perovskite: First-principles study, AIP Adv. **12**, 075122 (2022).

[54] J. Liang, P. Zhao, C. Wang, Y. Wang, Y. Hu, G. Zhu, L. Ma, J. Liu, and Z. Jin, CsPb$_{0.9}$Sn$_{0.1}$IBr$_2$ based all-inorganic perovskite solar cells with exceptional efficiency and stability, J. Am. Chem. Soc. **139**, 14009 (2017).

[55] W. van der Stam, J. J. Geuchies, T. Altantzis, K. H. W. van den Bos, J. D. Meeldijk, S. Van Aert, S. Bals, D. Vanmaekelbergh, and C. de Mello Donega, Highly emissive divalent-ion-doped colloidal CsPb$_{(1--x)}$M$_x$Br$_3$ perovskite nanocrystals through cation exchange, J. Am. Chem. Soc. **139**, 4087 (2017).

[56] Y. Su, K.-K. Song, M. Zhong, L.-B. Shi, and P. Qian, Stability and phonon-limited mobility for CsSnI$_3$ and CsPbI$_3$, J. Jallcom **889**, 161723 (2021).

[57] I. S. Torres, J. L. F. Da Silva, and M. P. Lima, The role of M^{3+} substitutional doping (M = In, Sb, Bi) in the passivation of the α-CsPbI$_3$(100) surface, J. Phys. Chem. C **127**, 1713 (2023).

[58] I. Deretzis, C. Bongiorno, G. Mannino, E. Smecca, S. Sanzaro, S. Valastro, G. Fisicaro, A. La Magna, and A. Alberti, Exploring the structural competition between the black and the yellow phase of CsPbI$_3$, Nanomaterials **11**, 1282 (2021).

[59] S. Masi, A. F. Gualdrón-Reyes, and I. Mora-Seró, Stabilization of black perovskite phase in FAPbI$_3$ and CsPbI$_3$, ACS Energy Lett. **5**, 1974 (2020).

[60] M. P. Lima, L. Cabral, E. Margapoti, S. Mahapatra, J. L. F. Da Silva, F. Hartmann, S. Höfling, G. E. Marques, and V. Lopez-Richard, Defect-induced magnetism in II-VI quantum dots, Phys. Rev. B **99**, 014424 (2019).

[61] L. Cabral, V. Lopez-Richard, J. L. Da Silva, G. Marques, M. P. Lima, Y. Onofre, M. Teodoro, and M. de Godoy, Insights into the nature of optically active defects of ZnO, J. Lumin. **227**, 117536 (2020).

[62] W. Travis, E. N. K. Glover, H. Bronstein, D. O. Scanlon, and R. G. Palgrave, On the application of the tolerance factor to inorganic and hybrid halide perovskites: a revised system, Chem. Sci. **7**, 4548 (2016).

[63] L. Fu, Y. Zhang, B. Chang, B. Li, S. Zhou, L. Zhang, and L. Yin, A fluorine-modulated bulk-phase heterojunction and tolerance factor for enhanced performance and structure stability of cesium lead halide perovskite solar cells, J. Mater. Chem. A **6**, 13263 (2018).

[64] G. Wang, M. Lei, J. Liu, Q. He, and W. Zhang, Improving the stability and optoelectronic properties of all inorganic less-Pb

[65] perovskites by B-site doping for high-performance inorganic perovskite solar cells, Solar RRL **4**, 2000528 (2020).

[65] J. Varignon, M. Bibes, and A. Zunger, Origins versus fingerprints of the Jahn-Teller effect in d-electron ABX$_3$ perovskites, Phys. Rev. Res. **1**, 033131 (2019).

[66] A. C. Dias, M. P. Lima, and J. L. F. Da Silva, Role of structural phases and octahedra distortions in the optoelectronic and excitonic properties of CsGeX$_3$ (X = Cl, Br, I) perovskites, J. Phys. Chem. C **125**, 19142 (2021).

[67] I. Leonov, N. Binggeli, D. Korotin, V. I. Anisimov, N. Stojić, and D. Vollhardt, Structural relaxation due to electronic correlations in the paramagnetic insulator KCuF$_3$, Phys. Rev. Lett. **101**, 096405 (2008).

[68] A. N. Christensen, S. E. Rasmussen, P. Karvonen, A. Kjær, R. H. Shapiro, and A. Westerdahl, A ferroelectric chloride of perowskite type. Crystal structure of CsGeCl$_3$, Acta Chem. Scand. **19**, 421 (1965).

[69] K. M. Hossain, M. Z. Hasan, and M. L. Ali, Narrowing band gap and enhanced mechanical and optoelectronic properties of perovskite halides: Effects of metal doping, AIP Adv. **11**, 015052 (2021).

[70] L. Zhang, F. Yao, J. Meng, W. Zhang, H. Wang, X. Liu, J. Meng, and H. Zhang, Oxygen migration and proton diffusivity in transition-metal (Mn, Fe, Co, and Cu) doped Ruddlesden–Popper oxides, J. Mater. Chem. A **7**, 18558 (2019).

[71] M. N. Islam, J. Podder, and M. L. Ali, The effect of metal substitution in CsSnI$_3$ perovskites with enhanced optoelectronic and photovoltaic properties, RSC Adv. **11**, 39553 (2021).

[72] C.-H. Chien, S. H. Chiou, G. Guo, and Y.-D. Yao, Electronic structure and magnetic moments of 3d transition metal-doped ZnO, J. Magn. Magn. Mater. **282**, 275 (2004).

[73] Q. Yao, C. Tian, Z. Lu, J. Wang, H. Zhou, and G. Rao, Antiferromagnetic-ferromagnetic transition in Bi-doped LaFeO$_3$ nanocrystalline ceramics, Ceram. Int. **46**, 20472 (2020).

[74] Q. Yang, X. Hu, X. Shen, A. V. Krasheninnikov, Z. Chen, and L. Sun, Enhancing ferromagnetism and tuning electronic properties of CrI$_3$ monolayers by adsorption of transition-metal atoms, ACS Appl. Mater. Interfaces **13**, 21593 (2021).

[75] P. Lv, Y.-L. Li, and J.-F. Wang, Monolayer Ti$_2$C MXene: manipulating magnetic properties and electronic structures by an electric field, Phys. Chem. Chem. Phys. **22**, 11266 (2020).

[76] M. Jamal, S. S. Nishat, and A. Sharif, Effects of transition metal (Fe, Co and Ni) doping on structural, electronic and optical properties of CuO: DFT+U study, Chem. Phys. **545**, 111160 (2021).

[77] Y. R. Wang, S. Li, and J. B. Yi, Transition metal-doped tin monoxide monolayer: A first-principles study, J. Am. Chem. Soc. **122**, 4651 (2018).